



HAL
open science

Enhanced Photon Extraction from a Nanowire Quantum Dot Using a Bottom-Up Photonic Shell

Mathieu Jeannin, Thibault Cremel, Teppo Häyrynen, Niels Gregersen, Edith Bellet-Amalric, Gilles Nogues, Kuntheak Kheng

► **To cite this version:**

Mathieu Jeannin, Thibault Cremel, Teppo Häyrynen, Niels Gregersen, Edith Bellet-Amalric, et al.. Enhanced Photon Extraction from a Nanowire Quantum Dot Using a Bottom-Up Photonic Shell. Physical Review Applied, 2017, 8 (5), pp.054022. 10.1103/PhysRevApplied.8.054022 . hal-01635907

HAL Id: hal-01635907

<https://hal.science/hal-01635907>

Submitted on 15 Nov 2017

HAL is a multi-disciplinary open access archive for the deposit and dissemination of scientific research documents, whether they are published or not. The documents may come from teaching and research institutions in France or abroad, or from public or private research centers.

L'archive ouverte pluridisciplinaire **HAL**, est destinée au dépôt et à la diffusion de documents scientifiques de niveau recherche, publiés ou non, émanant des établissements d'enseignement et de recherche français ou étrangers, des laboratoires publics ou privés.

1 **Enhanced photon extraction from a nanowire quantum dot using a**
2 **bottom-up photonic shell**

3 Mathieu Jeannin,^{1,*} Thibault Cremel,^{2,*} Teppo Häyrynen,³ Niels
4 Gregersen,³ Edith Bellet-Amalric,² Gilles Nogues,^{1,†} and Kuntheak Kheng²

5 ¹*Univ. Grenoble Alpes, CNRS, Institut Néel, "Nanophysique*
6 *et semiconducteurs" group, F-38000 Grenoble, France*

7 ²*Univ. Grenoble Alpes, CEA, INAC, PHELIQS, "Nanophysique*
8 *et semiconducteurs" group, F-38000 Grenoble, France*

9 ³*DTU Fotonik, Department of Photonics Engineering, Technical University of*
10 *Denmark, Ørsteds Plads, Building 343, DK-2800 Kongens Lyngby, Denmark*

11 **Abstract**

12 Semiconductor nanowires offer the possibility to grow high quality quantum dot heterostructures,
13 and in particular CdSe quantum dots inserted in ZnSe nanowires have demonstrated the ability to
14 emit single photons up to room temperature. In this letter, we demonstrate a bottom-up approach
15 to fabricate a photonic fiber-like structure around such nanowire quantum dots by depositing an
16 oxide shell using atomic layer deposition. Simulations suggest that the intensity collected in our
17 NA=0.6 microscope objective can be increased by a factor 7 with respect to the bare nanowire
18 case. Combining micro-photoluminescence, decay time measurements and numerical simulations,
19 we obtain a 4-fold increase in the collected photoluminescence from the quantum dot. We show
20 that this improvement is due to an increase of the quantum dot emission rate and a redirection of
21 the emitted light. Our ex-situ fabrication technique allows a precise and reproducible fabrication
22 on a large scale. Its improved extraction efficiency is compared to state of the art top-down devices.

* contributed equally to this work

† gilles.nogues@neel.cnrs.fr

23 I. INTRODUCTION

24 Controlling and enhancing the spontaneous emission of quantum emitters is one of the
25 current key issues in the field of nanophotonics. Semiconductor quantum dots (QDs) are
26 considered as promising and efficient single-photon emitters for quantum optics applications.
27 [1–6] Over the past few years, several approaches have been pursued to control their emis-
28 sion properties, from the use of photonic crystals [7, 8] to top-down photonic wires [9–11]
29 and trumpets.[12, 13] These strategies are based on the early work of Purcell[14] which
30 demonstrated that the spontaneous emission of an emitter can be modified by engineering
31 its electromagnetic environment. They rely on a waveguiding approach to increase the cou-
32 pling between a well-defined propagating optical mode and the QD while simultaneously
33 reducing the coupling between the QD and background radiation modes, offering control of
34 both the optical mode profile and the QD spontaneous emission rate.

35 In this context, the interest of the dot-in-a-nanowire configuration fabricated using
36 bottom-up methods naturally arises because it provides a simple way to ensure the center-
37 ing of a single quantum emitter in the photonic structure.[15–17] The bottom-up fabrication
38 method also avoids heavy processing, like etching the semiconducting material, that is often
39 detrimental to the QDs optical properties. However, the main realizations up to now concern
40 III-V semiconductors, [15–17] limiting the operation range to the cryogenic temperature.
41 Tackling this issue, the potential of II-VI materials, in particular CdSe QDs inserted inside
42 ZnSe nanowires (NWs) has been demonstrated in previous studies. They allow for robust
43 high temperature single-photon emission using heteroepitaxial [18] or homoepitaxial [19]
44 nanowire growth. Contrary to all the aforementioned systems where the photonic wire
45 structure has a diameter comparable to the wavelength λ/n of the guided light which allows
46 for highly efficient coupling to the HE_{11} mode[20], the diameter of the II-VI NW embedding
47 the QD (~ 20 nm) is much smaller than the wavelength of the emitted light (530 nm). It
48 leads to light emission predominantly into non-guided radiation modes and a low collection
49 efficiency. An additional fabrication effort has thus to be made to ensure an efficient coupling
50 to the collection optics.

51 In a previous report[21] we have theoretically investigated the potential of using an oxide
52 shell deposition on a bare ZnSe NW to form a thick photonic wire structure. In this article,
53 we experimentally demonstrate the use of atomic layer deposition (ALD) to fabricate a

54 conformal aluminum oxide (Al_2O_3) shell around ZnSe NWs containing a single CdSe QD.
 55 We show that the oxide shell drastically enhances the light intensity emitted by the QD, and
 56 we use time-resolved microphotoluminescence to systematically study the effect of the shell
 57 thickness on the nanowire quantum dot (NWQD) emission rate. Our results are compared
 58 to numerical simulations accounting for the real NW geometry, evidencing the different
 59 physical mechanisms leading to the enhancement of the spontaneous emission from the QD
 60 and to the improved light collection from the emitting structure.

61 II. PRINCIPLES OF OPERATION

62 To illustrate the effect of the NW and its surrounding medium on the QD emission rate,
 63 let us consider a QD placed inside an infinitely long cylinder as illustrated in Fig. 1(a)
 64 radiating a field at a wavelength λ . The cylinder is made of a dielectric material (refractive
 65 index n) and has a diameter d . We first consider a dipole orientation perpendicular to the
 66 NW axis in order to use the NW as a propagation medium for the emitted light. In the limit
 67 where $d \ll \lambda/n$, the dielectric screening effect[11] reduces the spontaneous emission rate γ
 68 by a factor:

$$\frac{\gamma}{\gamma_0} = \frac{4}{n(n^2 + 1)^2}, \quad (1)$$

69 where γ_0 is the radiative emission rate in the bulk material of index n . [22] For a ZnSe cylinder
 70 ($n_{\text{ZnSe}} = 2.68$ at $\lambda=530$ nm), the screening factor is $\sim 1/45$. If the NW is surrounded by a
 71 shell of refractive index n_s instead of vacuum, equation 1 remains valid by replacing n with
 72 the index contrast n/n_s . For an Al_2O_3 surrounding medium ($n_s = 1.77$), the screening factor
 73 becomes $\sim 1/4.1$, resulting in an order of magnitude larger radiative rate.

74 In addition to changing the dielectric screening, the Al_2O_3 shell also influences the guiding
 75 of light along the NW. We have computed the total emission rate γ and the emission rate
 76 $\gamma_{\text{HE}_{11}}$ into the fundamental HE_{11} waveguide mode from a radial dipole as function of the shell
 77 thickness t_s [see Fig. 1(a)] using a semi-analytical approach[23] combined with an efficient
 78 non-uniform discretization scheme in k space.[24] The results are plotted in Figure 1(b). We
 79 observe that the shell thickness of ~ 120 nm not only leads to an increased total emission
 80 rate, it also allows for confinement of the fundamental HE_{11} mode to the core-shell NW
 81 leading to a preferential coupling of the emitted light to this mode. Figure 1(c) presents the
 82 spontaneous emission β factor representing the fraction $\beta = \gamma_{\text{HE}_{11}}/\gamma$ of emitted light coupled

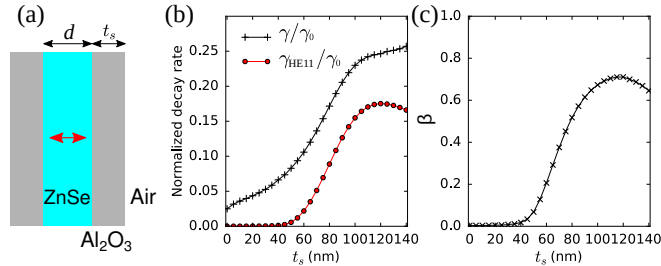


Figure 1. (a) Geometry of the infinite NW. (b) Total spontaneous emission rate (black +) and spontaneous emission rate into the first guided mode HE_{11} (red •) as a function of shell radius for a radial dipole. (c) Fraction β of power radiated into the HE_{11} mode.

83 to the HE_{11} mode. We observe indeed that up to 71% of the emitted light is coupled to this
 84 mode for $t_s=120$ nm. The dipole thus becomes coupled to the equivalent of a monomode
 85 photonic wire[9–11, 15–17] paving the way to the control of its far-field radiation pattern.

86 III. SAMPLE FABRICATION

87 Our emitters are CdSe QDs embedded inside a ZnSe NW with a thin, epitaxial passivation
 88 $Zn_{0.83}Mg_{0.17}Se$ shell grown around the NW. They are grown by molecular beam epitaxy on a
 89 GaAs(111)B substrate. A ZnSe buffer layer is first grown on the GaAs substrate after which
 90 a thin layer of Au (less than one monolayer thick) is evaporated on the sample surface and
 91 dewetted at 510 °C to form small (~ 10 nm diameter) Au droplets that serve as a catalyst
 92 for the NW growth. The substrate temperature is then set at 400 °C and a flux of Zn and Se
 93 atoms with an excess of Se is used, inducing preferential growth of vertical ZnSe NWs. The
 94 NWs are in wurtzite phase and their diameter is the same as the droplet (~ 10 nm diameter).
 95 The thickness of the initial Au layer is chosen to ensure a low NW density (≤ 1 NW per
 96 μm^2). After the growth of a 400 nm high NW, the atom fluxes are stopped to allow the
 97 evacuation of residual Se atoms inside the droplet. Then, the QD is grown under a flux of Cd
 98 and Se atoms for 20 s. The fluxes are interrupted again before the ZnSe growth is resumed,
 99 resulting in an expected QD height of 2-3 nm inserted in a ~ 700 nm high NW. Finally, an
 100 epitaxial $Zn_{0.83}Mg_{0.17}Se$ shell (5 nm thick) is grown around the NW at 220 °C. A scanning
 101 electron microscope (SEM) image of such a CdSe/ZnSe/ZnMgSe core/shell NWQD system
 102 is presented in Figure 2(a). The flag-shape termination of the NW is formed during the

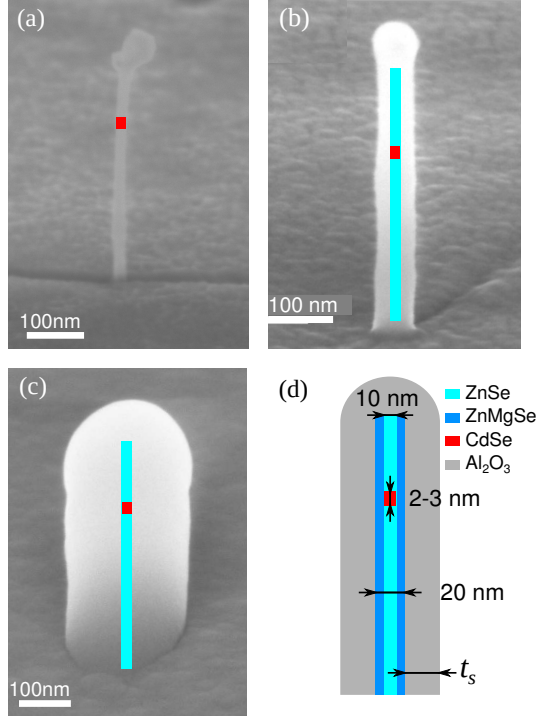


Figure 2. (a) SEM image of a standing ZnSe/ZnMgSe NW embedding a CdSe QD. The QD position is marked by the red square. (b,c) Tilted SEM image of a ZnSe NW after a 20 nm and 110 nm thick Al₂O₃ shell deposition respectively. The NW is sketched on the SEM image. Note the circular shape of the shell as well as its hemispherical termination above the NW apex. (d) Sketch of the NWQD geometry, indicating the QD height (2-3 nm), the NW diameter ($\simeq 10$ nm), the epitaxial shell thickness ($\simeq 5$ nm) and the ALD shell thickness t_s .

103 growth of the ZnMgSe shell. It is present in some NWs.

104 The higher bandgap of Zn_{0.83}Mg_{0.17}Se shell prevents the charge carriers to recombine
 105 non-radiatively on the ZnSe NW sidewall and hence improves the quantum yield of the
 106 CdSe emitter. In principle, it could directly be used to grow a photonic wire of diameter
 107 $\sim \lambda/n_{\text{ZnSe}}$ around the NWQD. However, during the epitaxial shell growth two phenomena
 108 are competing: the radial growth of the shell around the wurtzite NWs, and the vertical
 109 growth of a 2D Zn_{0.83}Mg_{0.17}Se layer on the sample surface. The radial shell growth rate is
 110 very low because the growth of ZnSe on WZ surfaces is not favourable. Because of this low
 111 shell growth rate, a trade-off has to be found to avoid burying the NWs in a Zn_{0.83}Mg_{0.17}Se
 112 matrix. As a result, only thin epitaxial shells can be fabricated.

113 The complexity of creating a thick epitaxial shell is one of the reasons why we fabricate

114 the photonic structure by depositing an oxide shell around the NW using ALD. Another
 115 reason is that, since this process step can be done *separately* from the NW growth process,
 116 it allows to tune ex situ the shell parameters after a first optical characterization of the
 117 QD. Indeed, due to its slow deposition rate, the ALD process allows to precisely control the
 118 deposited thickness, which can also be finally verified using scanning electron microscopy.
 119 We have tested several oxide materials, and selected Al_2O_3 because it produced very smooth
 120 and conformal, amorphous shells. Figure 2(b) and (c) show two SEM images of the result-
 121 ing oxide shell deposition (20 nm and 110 nm), and the complete structure is sketched in
 122 Fig. 2(d). We note that the conformal deposition allows to end the NW+shell structure by
 123 an almost perfect half-sphere as can be seen in Fig. 2(b,c). ALD also buries the Au droplet
 124 under the shell. The latter might interact with the field emitted by the QD through its
 125 localized plasmon resonance. Considering its small diameter it will essentially absorb the
 126 incoming field. Moreover the guided HE11 mode profile presents a minimum on the NW
 127 axis. This is why we neglect the droplet influence in the following.

128 IV. EXPERIMENTAL RESULTS

129 A sample from a single epitaxial growth process is cut in pieces, and photonic structures
 130 with different oxide shell thicknesses are fabricated. Taking advantage of the low NW den-
 131 sity, individual structures are optically characterized directly on the growth substrate. The
 132 samples are mounted on the cold finger of a He-flux cryostat and cooled down to 4 K. Indi-
 133 vidual photonic structures are probed using confocal microphotoluminescence (μPL). They
 134 are excited by a supercontinuum pulsed laser (Fianium WhiteLase, 10 ps pulse duration,
 135 repetition rate 76 MHz) and a spectrometer selecting a 10 nm bandwidth centered around
 136 485 nm. This excitation energy, below the ZnSe gap, allows us to induce crossed transitions
 137 between delocalized states in the NW 1D continuum and a discrete confined 0D state in the
 138 NWQD band structure[25]. In this configuration, the NW axis is aligned with the optical
 139 axis and emission from the QD is collected by a $NA = 0.6$ objective. A typical NWQD
 140 spectrum is presented in Figure 3(a) as a function of the pump laser power. Three lines
 141 can be identified and are attributed to the exciton (X), the charged exciton (CX) and the
 142 bi-exciton (XX) respectively. The total emission intensity of the X line as a function of the
 143 pump power is reported in Figure 3(b). It shows a linear increase at low pumping power, and

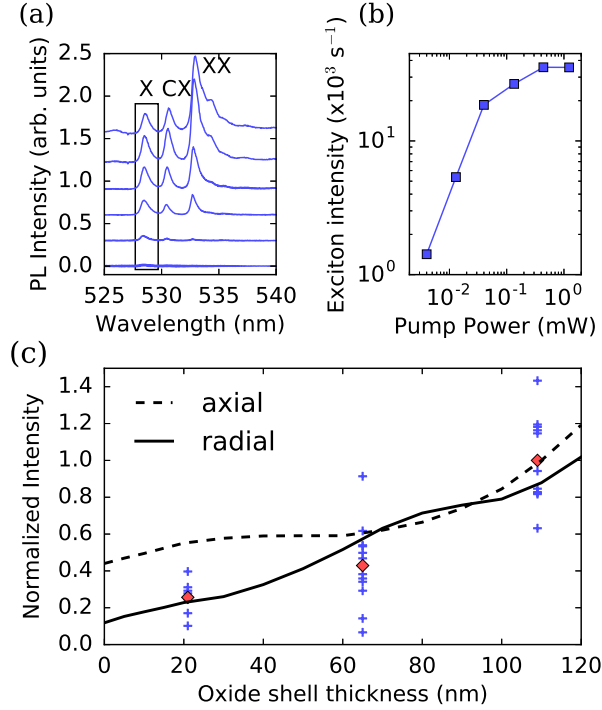


Figure 3. (a) μ PL spectrum of a NWQD with 120 nm thick photonic shell for different pumping powers. It shows a exciton (X), charged exciton (CX) and biexciton (XX) lines. The corresponding pumping powers are reported in panel (b). The black rectangle indicates the integration bandwidth used to extract the total exciton emission intensity (X line). (b) Integrated exciton emission intensity as a function of pumping power, in a log-log scale. (c) Blue crosses: Total exciton emission intensity for different NWQDs as a function of the oxide shell radius. Red diamonds: average of the experimental data points. Data are normalized to the average intensity at $t_s = 110$ nm Black lines: results of the numerical simulations for a radial (solid line) and an axial (dashed line) dipole. They are normalized to the axial intensity at $t_s = 110$ nm

144 a constant plateau at high pumping powers corresponding to the saturation of the exciton
145 level.[26] Under pulsed excitation, we note that changing the shell thickness might modify
146 the laser power in the NW and the excitation probability of the QD. Hence it affects the
147 slope at low power in Fig. 3(b). It has however no effect on the saturation plateau which only
148 depends on the QD emission rate and light collection efficiency. This allows us to compare
149 statistical sets of nanostructures with different oxide shell thicknesses. The total integrated
150 emission at saturation as a function of the oxide shell thickness is reported in blue markers
151 for each NWQD in Figure 3(c). The values have been normalized to the average intensity

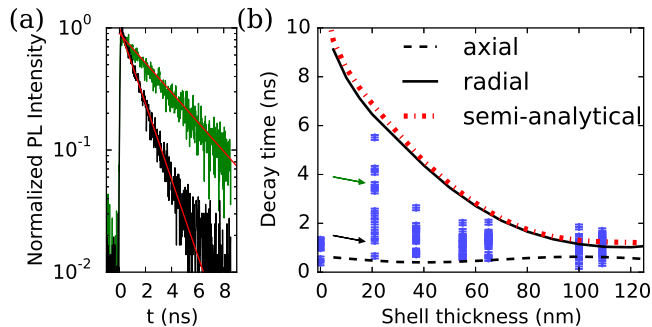


Figure 4. (a) Example of TRPL signal versus time for 2 NWs with a $t_s=20$ nm shell. Background counts are measured for $t < 0$ and subtracted. Amplitude of counts are normalized to 1 to compare the 2 datasets. Red lines are mono-exponential fits, whose corresponding points in (b) are shown by arrows. (b) Blue crosses: experimental exciton decay times for several QDs as a function of the oxide shell radius. The vertical error bars represent the fit error. Black lines: numerical simulation results for a radial dipole (solid line), or an axial dipole (dashed line). Red dashed-dotted line: Semi-analytical calculations for the infinite NW.

152 at $t_s = 110$ nm. For NWs without an oxide shell, the luminescence intensity is very low and
 153 we were never able to reach the saturation regime, this is why we do not report the corre-
 154 sponding points in Fig. 3(c). For each shell thickness, we observe a large spread in exciton
 155 saturation intensity. However, we note a general trend of increasing saturation intensity
 156 with increasing shell thickness, as demonstrated by the red markers which show the position
 157 of the average intensity of our measurements for each shell thickness. On average, the de-
 158 position of a 110 nm thick shell results in the experiments in an almost 4-fold enhancement
 159 of the collected intensity with respect to the 20 nm thick shell case. The semi-analytical
 160 calculations show that this enhancement is 10-fold when we compare to a NW without oxide
 161 shell.

162 The observed increase in intensity at saturation corresponds to the combination of im-
 163 proved collection efficiency through light redirection from the structure and enhancement
 164 of the spontaneous emission rate. In the latter case, a modification of the QD dynamics is
 165 expected to be detected by measuring the exciton decay rate. Time-resolved measurements
 166 were carried out using a low pump power as compared to the exciton saturation power to
 167 avoid any repopulation of the X level. The measured decay transients are thus monoex-
 168 ponential. The fitted decay constant is the total exciton decay time τ . The experiment

169 was carried out in another setup on a different set of photonic structures compared to the
 170 one of figure 3(c). The same excitation laser was used, the QD fluorescence was spectrally
 171 filtered in a spectrometer (500gr/mm grating) and integrated on an avalanche photodiode
 172 in a photon correlation setup, using the exit slit of the spectrometer as a spectral bandpass
 173 filter. The results of these measurements, presented in Figure 4 show also a great dispersion
 174 in decay time. One observes however that longer lifetimes are observed for smaller shell
 175 thickness (up to 5.9 ns). Increasing the shell thickness leads to an overall decrease in the
 176 measured exciton lifetime, hence an enhancement of the exciton decay rate in agreement
 177 with the results of the numerical simulations. For systems without an oxide shell, only a
 178 few NWQDs give a large enough signal to be properly measured. They yield a much smaller
 179 dispersion of short decay times.

180 V. DISCUSSION AND COMPARISON TO NUMERICAL SIMULATIONS

181 A. Dispersion of the results

182 For each oxide shell thickness, the large variations of the experimental results in both
 183 Figs. 3(c) and 4 have several possible origins. First, the presence of non-radiative recom-
 184 bination channels can reduce the intensity at saturation and change the decay time. The
 185 non-radiative recombination rate can vary from QD to QD because of fabrication inhomo-
 186 geneities, leading to a spread in the measured values.[27] Second, variations in the QD aspect
 187 ratio and piezoelectric fields induced internal strain applied by both the ZnSe core and the
 188 $\text{Zn}_{0.83}\text{Mg}_{0.17}\text{Se}$ shell lead to different overlap of electron and hole wavefunctions and hence
 189 different exciton oscillator strengths. Finally, considering the QD aspect ratio and internal
 190 strain, we expect a heavy-hole exciton type for our QDs.[28–31] Heavy-hole exciton recom-
 191 bination results in a mixture of circularly polarized emission, composed of two degenerate
 192 out-of-phase radial dipoles. However, strain and confinement effects might lead to valence
 193 band mixing between light hole and heavy hole levels,[32–34] resulting in an emission com-
 194 posed of a mixture between axial and radial dipoles and hence to a spread in total emitted
 195 intensity, as we discuss later. Additional measurements on NWQDs grown in similar condi-
 196 tions and mechanically dispersed on a substrate (i.e. lying horizontally on it) revealed that
 197 one NWQD out of 6 emit light polarized along the NW axis, while others emit light polarized

198 perpendicularly to the NW axis, evidencing the presence of both kinds of dipoles. Due to
 199 the $\text{Zn}_{0.83}\text{Mg}_{0.17}\text{Se}$ shell and low temperature of observation, we expect that non-radiative
 200 effects play a minor role. The epitaxial shell prevents non-radiative decay channels owing
 201 to surface traps. Additional measurements as a function of temperature show that both
 202 the emission intensity and the decay time do not change significantly up to 150-200 K (not
 203 presented here). This indicates that the non-radiative effects are not dominating at low
 204 temperature, as in the present experiment. While we cannot yet completely rule out the
 205 contribution of non-radiative effects, we think that the major effect to explain the dispersion
 206 of the results comes from variations in valence band mixing and oscillator strength due to
 207 the local environment of the QD. Finally let us stress that the shortest decay times (1-2 ns)
 208 we measure remain longer than the decay time of CdSe self-assembled QD embedded in
 209 bulk ZnSe (<1 ns)[35]. The reduction of the dielectric screening effect is a main effect we
 210 evidence.

211 B. Collected intensity and radiative lifetime

212 To better understand the effect of the shell deposition on the NWQD emission, we perform
 213 numerical simulations of the photonic structure formed by the full NW + oxide shell geom-
 214 etry [see Fig. 2(d)]. It takes into account the presence of the ZnSe substrate, and the Al_2O_3
 215 shell and layer deposited on the NWs and substrate. The QD is modeled as an oscillating
 216 electric dipole, either in the axial direction (along the NW axis) or in the radial direction
 217 (orthogonal to the NW axis). We perform finite-element method simulations (Comsol v4.1)
 218 to compute the total field radiated by the dipole.[34] For each shell thickness and dipole
 219 orientation, we evaluate the power radiated towards the objective by computing the flux of
 220 the Poynting vector over a surface limited by its numerical aperture (NA=0.6) in a region
 221 far from the NW where near field can be neglected. The results of these simulations are
 222 reported in Figure 3(c) in black lines for an axial (dashed line) or radial (solid line) dipole.
 223 The results are normalized to the axial intensity at $t_s = 110$ nm. Comparing the simulated
 224 integrated intensity in the case of a 20 nm and 110 nm reveals an enhancement factor less
 225 than 2-fold for an axial dipole and almost 4-fold for a radial dipole. The 4-fold enhancement
 226 observed in our measurements suggests that on average, the dominant emitting dipole in
 227 our structure is radial, in good agreement with the recombination of a heavy hole exciton.

228 The theoretical limits for the radiative lifetimes is extracted from the numerical sim-
 229 ulations by integrating the total power radiated over every direction for the two dipole
 230 orientations (radial and axial) P . We normalize this value by the same quantity computed
 231 for a dipole in bulk ZnSe P_0 . For a purely radiative system we have $P/P_0 = \gamma/\gamma_0 = \tau_0/\tau$ [36],
 232 where τ and τ_0 are the radiative lifetime for the nanostructure and for bulk ZnSe respectively.
 233 Radiative times are presented in black lines in Figure 4, where we have chosen $\tau_0 = 300$ ps
 234 in good agreement with previously reported radiative lifetime of CdSe QD in bulk ZnSe[37].
 235 The axial dipole radiates with an almost constant decay time as a function of the oxide shell
 236 thickness, while the radial dipole decay time strongly decreases with increasing oxide shell
 237 thickness t_s . Additionally, we compare the decay time for the radial dipole computed for the
 238 full geometry to the semi-analytical calculations for the infinite NW presented in fig. 1(b)
 239 with the same τ_0 value. The agreement is excellent indicating that interference effects due
 240 to reflections from the substrate and from the top hemispherical termination are negligible.

241 Comparing the trends of the simulations, we can confirm that our emitters bear a strong
 242 radial dipole character. The measurements dispersion can be well understood by considering
 243 that the real emitters are a mixture of radial and axial dipoles radiating with a characteristic
 244 decay time comprised between the simulated lifetimes of the pure radial and axial dipole.
 245 We do not observe long decay time for NWQDs without an oxide shell in Fig. 4. For these
 246 systems, it is very difficult to find emitters which are bright enough to be detected is because
 247 both the laser absorption and the emission rate of a radial dipole are very weak for such
 248 small NW diameters. We think that the emitters which have been selected correspond to
 249 NWQDs having a large fraction of axial dipole character as they are the brightest ones when
 250 no oxide shell is present.

251 C. Radiation pattern

252 To analyze the mechanisms leading to the increase in collected intensity with increasing
 253 shell thickness, we present in Figure 5 several simulated radiation patterns. They are rep-
 254 resented as polar plots of the far-field intensity $I(\theta)$ in the top (x, z) plane, θ is the angle
 255 between the direction of observation and the vertical z axis. Simulations are made using
 256 respectively a radial dipole [along x , Figures 5(a-c)] or an axial dipole [along z , Figures 5(d-
 257 f)].

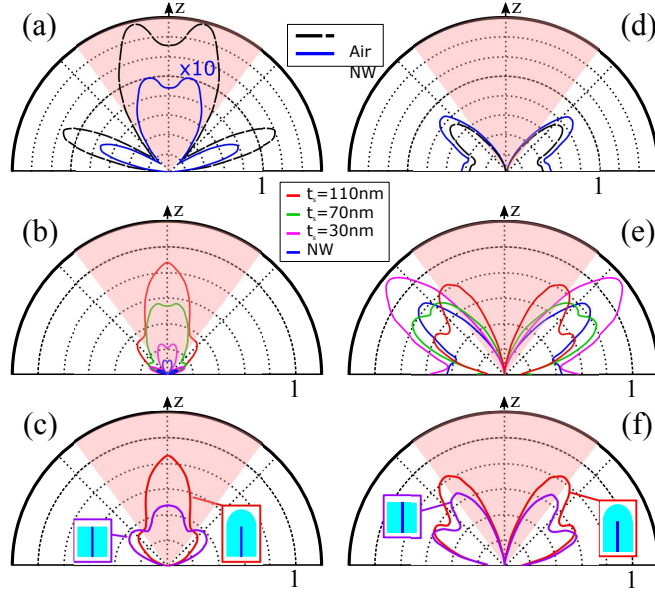


Figure 5. Radiation patterns from numerical simulations for a radial dipole placed at 470 nm above the substrate. The experimental NA region is shaded and indicated in red. (a,d) Comparison between the case of a free-standing emitter in air (black dashes), and embedded inside the NW (blue solid line) for a radial (a) or axial (d) dipole. They evidence the effect of the dielectric screening from the NW on the radial dipole and the absence of screening for the axial dipole. (b, e) Comparison of the total emitted intensity versus t_s for a radial (b) or axial (e) dipole. A combined effect of reduced dielectric screening and light guiding and redirection towards small angles is observed. (c, f) Effect of the shell layer termination shape for a radial (c) or axial (f) dipole. The hemispherical shape increases the fraction of light that is redirected towards the z direction.

258 Figures 5(a,d) show the effect of the NW structure alone (no oxide shell being present)
 259 on such dipoles by comparing it to the case of a free standing dipole in vacuum above
 260 the same ZnSe substrate. One can see that the presence of the NW does not affect the
 261 shape of radiation diagram, which is essentially determined by the interferences between the
 262 directly radiated field and its reflection on the substrate. Most remarkably, in the case of the
 263 radial dipole the presence of the NW dramatically reduces the emission intensity through
 264 the dielectric screening effect discussed earlier. Simulations show a radiative rate reduction
 265 by a factor $\sim 1/16 \simeq n_{\text{ZnSe}}/45$ in agreement with the dielectric screening value predicted by
 266 Eq. (1). In contrast, in the case of the axial dipole it can be seen that the presence of the
 267 NW only slightly increases the emitted intensity.

268 Figures 5(b,e) show the computed radiation patterns of the NWQD for increasing oxide
 269 shell thickness t_s . In the case of the radial dipole, the shell first reduces the index contrast
 270 between the NW and the surrounding medium (cf. Eq. 1), resulting in a strong reduction of
 271 the emitter lifetime and thus in an increased total emitted intensity as seen in in Fig. 3(c)
 272 and Fig. 4. Note that the the intensity pattern shown in the polar plot must be multiplied by
 273 the solid angle $\sin \theta d\theta$ if one wants to evaluate the power radiated in the numerical aperture.
 274 This is why the intensity for an axial dipole can be larger than for a radial one, as seen in
 275 Fig. 3(c). Second, as shown in Figure 1(c), the shell presence ensures preferential emission
 276 into the guided HE_{11} mode for increasing shell thickness. As a consequence a near-Gaussian
 277 far-field emission pattern corresponding to the far-field emission profile of the HE_{11} mode[38]
 278 is observed for $t_s=110$ nm, contrary to the structures with a smaller oxide shell thickness
 279 where one observes the presence of two closely-spaced lobes at small emission angles ($\pm 10^\circ$
 280 with respect to the z -axis). The resulting emission into the 0.6 NA cone is maximum for
 281 $t_s = 110$ nm, where the emission into the HE_{11} mode is nearly maximum [cf. Fig. 1(b)].
 282 The effect of the oxide shell thickness on the axial dipole is completely different. While the
 283 total emitted intensity does not vary much, and hence the emitter lifetime stays constant (as
 284 noted in Fig. 4), the light emitted by the axial dipole does not couple to the HE_{11} mode but
 285 is emitted exclusively into radiation modes. Thus the fraction of intensity emitted towards
 286 the collection lens increases only slightly as the oxide shell thickness increases [cf. Fig.5(e)].
 287 This intensity increase for the axial dipole also presented in Fig.3(c) is not due to a change
 288 in the spontaneous emission rate of the emitter, but rather to a slight redirection of the
 289 emitted light.

290 Finally, Figures 5(c,f) compare the actual hemispherical geometry of the oxide shell ter-
 291 mination to the flat end of a simple lateral shell. They show that the presence of the
 292 hemisphere is beneficial to the radiation pattern for both kinds of dipole. For the radial
 293 dipole, the hemisphere enables a near-adiabatic expansion of the HE_{11} mode[38] leading to
 294 a narrowing of the far-field emission pattern and an increased collection by the numerical
 295 aperture. The axial dipole benefits less from the hemispherical termination of the photonic
 296 structure since no light from this dipole is coupled to the HE_{11} mode. We also note that half
 297 of the emitted light propagates towards the growth substrate and due to the index-matching
 298 condition between the NW and the substrate, this light is predominantly lost.

299 In order to assess the performances of our device we compute the ratio η between the

300 power radiated into a 0.6 NA to the one radiated into the top air side hemisphere. This
 301 parameter is a good figure of merit for the antenna redirection effect although it cannot be
 302 directly related to the overall collection efficiency because of the power lost in the substrate.
 303 For our full photonic structure and a radial dipole one has $\eta \simeq 80\%$ for $t_s=110$ nm. This value
 304 reduces to $\simeq 66\%$ for a flat terminated core-shell photonic wire illustrating the importance of
 305 the adiabatic expansion of the HE_{11} guided mode at the end of the wire. For the dipole in the
 306 NW without shell $\eta \simeq 55\%$. We have also simulated a structure inspired by state-of-the-art
 307 devices fabricated by top-down methods in Ref. [9]. In this case we simulate a 110 nm oxide
 308 shell photonic wire where the hemispherical termination is replaced by a conical taper of
 309 Al_2O_3 whose radius progressively decreases from 120 to 10 nm in 1.5 μm . In this case one
 310 has $\eta \simeq 94\%$, showing that although beneficial our hemispherical termination is not optimal.

311 VI. CONCLUSION

312 In summary, we have presented a bottom-up approach to fabricate a dielectric antenna
 313 around a QD inserted inside a NW. This method allows for both reproducible and very
 314 precise fabrication of the structure on a large ensemble of emitters at once. It is based on the
 315 deposition of a thick oxide shell around the NW using atomic layer deposition. Experiments
 316 show a 4-fold enhancement of the QD photoluminescence shown in Fig. 3(c) between a
 317 20 nm and a 110 nm thick shell. Semi-analytical calculations and numerical simulations of
 318 the structure reveal that the oxide shell thickness strongly acts on the radial dipole emission
 319 through two main phenomena: the reduction of the dielectric screening, which increases the
 320 spontaneous emission rate from the QD, and the redirection of light through a waveguiding
 321 effect. Simulations suggest that the collected intensity is multiplied by a factor 7 with respect
 322 to the bare NW case. The fabrication process of the photonic shell is very simple and can be
 323 applied to QDs emitting single photons up to room temperature. Although not optimal, the
 324 resulting structure is a step towards the best nanowire single photon sources operating at
 325 low temperature[9]. Dielectric screening could be further reduced by growing an oxide shell
 326 of higher index matching n_{ZnSe} like TiO_2 . We note also that in our system a large fraction
 327 of the emitted power is radiated in the substrate. This loss channel could be reduced by
 328 having a mirror at the bottom of the structure.[15, 39] Moreover, to fully benefit from the
 329 waveguiding approach, a better control on the intrinsic QD properties has to be reached

330 to ensure the presence of radial dipoles, which radiate more efficiently in the experimental
331 collection aperture.

332 ACKNOWLEDGMENTS

333 This work was supported by the French National Research Agency under the contract
334 ANR-10-LABX-51-01 and the Danish Research Council for Technology and Production (LO-
335 QIT Sapere Aude grant DFF #4005-00370).

-
- 336 [1] P. Michler, A. Kiraz, C. Becher, W. V. Schoenfeld, P. M. Petroff, L. Zhang, E. Hu, and
337 A. Imamoglu, “A quantum dot single-photon turnstile device,” *Science* **290**, 2282–2285 (2000).
338 [2] Charles Santori, Matthew Pelton, Glenn Solomon, Yseulte Dale, and Yoshihisa Yamamoto,
339 “Triggered single photons from a quantum dot,” *Phys. Rev. Lett.* **86**, 1502 (2001).
340 [3] Charles Santori, David Fattal, Jelena Vučković, Glenn S. Solomon, and Yoshihisa Yamamoto,
341 “Indistinguishable photons from a single-photon device,” *Nature* **419**, 594–597 (2002).
342 [4] A. Zrenner, E. Beham, S. Stufler, F. Findeis, M. Bichler, and G. Abstreiter, “Coherent proper-
343 ties of a two-level system based on a quantum-dot photodiode,” *Nature* **418**, 612–614 (2002).
344 [5] N. Akopian, N. H. Lindner, E. Poem, Y. Berlatzky, J. Avron, D. Gershoni, B. D. Ger-
345 ardot, and P. M. Petroff, “Entangled photon pairs from semiconductor quantum dots,”
346 *Phys. Rev. Lett.* **96**, 130501 (2006).
347 [6] Andrew J. Shields, “Semiconductor quantum light sources,” *Nature Photon.* **1**, 215 (2007).
348 [7] E. Viasnoff-Schwoob, C. Weisbuch, H. Benisty, S. Olivier, S. Varoutsis, I. Robert-Philip,
349 R. Houdré, and C. J. M. Smith, “Spontaneous emission enhancement of quantum dots in
350 a photonic crystal wire,” *Phys. Rev. Lett.* **95**, 183901 (2005).
351 [8] T. Lund-Hansen, S. Stobbe, B. Julsgaard, H. Thyrrerstrup, T. Süner, M. Kamp, A. Forchel,
352 and P. Lodahl, “Experimental realization of highly efficient broadband coupling of single quan-
353 tum dots to a photonic crystal waveguide,” *Phys. Rev. Lett.* **101**, 113903 (2008).
354 [9] Julien Claudon, Joël Bleuse, Nitin Singh Malik, Maela Bazin, P. Verine Jaffrennou,
355 Niels Gregersen, Christophe Sauvan, Philippe Lalanne, and Jean-Michel Gérard, “A
356 highly efficient single-photon source based on a quantum dot in a photonic nanowire,”

- 357 Nature Photon. **4**, 174–177 (2010).
- 358 [10] J. Heinrich, A. Huggenberger, T. Heindel, S. Reitzenstein, S. Höfling, L. Worschech, and
359 A. Forchel, “Single photon emission from positioned GaAs/AlGaAs photonic nanowires,”
360 Appl. Phys. Lett. **96**, 211117 (2010).
- 361 [11] Joël Bleuse, Julien Claudon, Megan Creasey, Nitin S. Malik, Jean-Michel Gérard, Ivan Maksy-
362 mov, Jean-Paul Hugonin, and Philippe Lalanne, “Inhibition, enhancement, and control of
363 spontaneous emission in photonic nanowires,” Phys. Rev. Lett. **106**, 103601 (2011).
- 364 [12] Mathieu Munsch, Julien Claudon, Joël Bleuse, Nitin S. Malik, Emmanuel Dupuy, Jean-Michel
365 Gérard, Yuntian Chen, Niels Gregersen, and Jesper Mørk, “Linearly polarized, single-mode
366 spontaneous emission in a photonic nanowire,” Phys. Rev. Lett. **108**, 077405 (2012).
- 367 [13] Mathieu Munsch, Nitin S. Malik, Emmanuel Dupuy, Adrien Delga, Joël Bleuse, Jean-Michel
368 Gérard, Julien Claudon, Niels Gregersen, and Jesper Mørk, “Dielectric gaas antenna ensuring
369 an efficient broadband coupling between an inas quantum dot and a gaussian optical beam,”
370 Phys. Rev. Lett. **110**, 177402 (2013).
- 371 [14] E.M. Purcell, “Spontaneous emission probabilities at radio frequencies,” in
372 *Proceedings of the American Physical Society*, Vol. 69 (American Physical Society (APS),
373 1946) p. 674.
- 374 [15] Michael E. Reimer, Gabriele Bulgarini, Nika Akopian, Moïra Hocevar, Maaïke Bouwes Bavinck,
375 Marcel A. Verheijen, Erik P.A.M. Bakkers, Leo P. Kouwenhoven, and Val Zwiller, “Bright
376 single-photon sources in bottom-up tailored nanowires,” Nature Comm. **3**, 737 (2012).
- 377 [16] Gabriele Bulgarini, Michael E. Reimer, Tilman Zehender, Moïra Hocevar, Erik P. A. M.
378 Bakkers, Leo P. Kouwenhoven, and Valery Zwiller, “Spontaneous emission control of single
379 quantum dots in bottom-up nanowire waveguides,” Appl. Phys. Lett. **100**, 121106 (2012).
- 380 [17] G. Bulgarini, M. E. Reimer, M. B. Bavinck, K. D. Jöns, D. Dalacu, P. J. Pool, E. P. Bakkers,
381 and V. Zwiller, “Nanowire waveguide launching single photons in a gaussian mode for ideal
382 fiber coupling,” Nano Lett. **14**, 4102–4106 (2014).
- 383 [18] Adrien Tribu, Gregory Sallen, Thomas Aichele, Régis André, Jean-Philippe Poizat, Catherine
384 Bougerol, Serge Tatarenko, and Kuntheak Kheng, “A high-temperature single-photon source
385 from nanowire quantum dots,” Nano Lett. **8**, 4326–4329 (2008).
- 386 [19] S. Bounouar, M. Elouneg-Jamroz, M. den Hertog, C. Morchutt, E. Bellet-Amalric, R. An-
387 dré, C. Bougerol, Y. Genuist, J.-Ph. Poizat, S. Tatarenko, and K. Kheng, “Ultrafast room

- 388 temperature single-photon source from nanowire-quantum dots,” *Nano Lett.* **12**, 2977 (2012).
- 389 [20] Y.-R. Nowicki-Bringuier, R. Hahner, J. Claudon, G. Lecamp, P. Lalanne, and J.-M. Gérard,
390 “A novel high-efficiency single-mode single photon source,” *Ann. Phys.* **32**, 151 (2008).
- 391 [21] T. Cremel, M. Elouneq-Jamroz, E. Bellet-Amalric, L. Cagnon, S. Tatarenko, and K. Kheng,
392 “Bottom-up approach to control the photon outcoupling of a II-VI quantum dot with a photonic
393 wire,” *Phys. Status Solidi C* **11**, 1263 (2014).
- 394 [22] Julien Claudon, Niels Gregersen, Philippe Lalanne, and Jean-Michel Gérard, “Harness-
395 ing light with photonic nanowires: Fundamentals and applications to quantum optics,”
396 *ChemPhysChem* **14**, 2393–2402 (2013).
- 397 [23] A. Yariv, *Optical electronics in modern communications* (1997).
- 398 [24] Teppo Häyrynen, Jakob Rosenkrantz de Lasson, and Niels Gregersen, “Open-
399 geometry Fourier modal method: modeling nanophotonic structures in infinite domains,”
400 *J. Opt. Soc. Am. A* **33**, 1298 (2016).
- 401 [25] A. Vasanelli, R. Ferreira, and G. Bastard, “Continuous absorption background and decoherence
402 in quantum dots,” *Phys. Rev. Lett.* **89** (2002), 10.1103/physrevlett.89.216804.
- 403 [26] We note that single-photon emission is preserved if one integrates both the signal from the X
404 and CX lines.[?].
- 405 [27] Petr Stepanov, Adrien Delga, Xiaorun Zang, Joël Bleuse, Emmanuel Dupuy, Emanuel Peinke,
406 Philippe Lalanne, Jean-Michel Gérard, and Julien Claudon, “Quantum dot spontaneous emis-
407 sion control in a ridge waveguide,” *Appl. Phys. Lett.* **106**, 041112 (2015).
- 408 [28] J. D. Eshelby, “The determination of the elastic field of an ellipsoidal inclusion, and related
409 problems,” *Proc. R. Soc. A* **241**, 376–396 (1957).
- 410 [29] J. D. Eshelby, “The elastic field outside an ellipsoidal inclusion,”
411 *Proc. R. Soc. A* **252**, 561–569 (1959).
- 412 [30] M. Zieliński, “Fine structure of light-hole excitons in nanowire quantum dots,”
413 *Phys. Rev. B* **88**, 115424 (2013).
- 414 [31] David Ferrand and Joël Cibert, “Strain in crystalline core-shell nanowires,”
415 *Eur. Phys. J. Appl. Phys.* **67**, 30403 (2014).
- 416 [32] K. F. Karlsson, V. Troncale, D. Y. Oberli, A. Malko, E. Pelucchi, A. Rudra, and
417 E. Kapon, “Optical polarization anisotropy and hole states in pyramidal quantum dots,”
418 *Appl. Phys. Lett.* **89**, 251113 (2006).

- 419 [33] Catherine Tonin, Richard Hostein, Valia Voliotis, Roger Grousson, Aristide Lemaitre, and An-
420 thony Martinez, “Polarization properties of excitonic qubits in single self-assembled quantum
421 dots,” *Phys. Rev. B* **85**, 155303 (2012).
- 422 [34] Mathieu Jeannin, Alberto Artioli, Pamela Rueda-Fonseca, Edith Bellet-Amalric,
423 Kuntheak Kheng, Régis André, Serge Tatarenko, Joël Cibert, David Fer-
424 rand, and Gilles Nogues, “Light-hole exciton in a nanowire quantum dot,”
425 *Phys. Rev. B* **95** (2017), 10.1103/physrevb.95.035305.
- 426 [35] G. Bacher, R. Weigand, J. Seufert, V. D. Kulakovskii, N. A. Gippius, A. Forchel, K. Leonardi,
427 and D. Hommel, “Biexciton versus exciton lifetime in a single semiconductor quantum dot,”
428 *Phys. Rev. Lett.* **83**, 4417–4420 (1999).
- 429 [36] L. Novotny and B. Hecht, *Principles of Nano-Optics*, 2nd ed. (2012).
- 430 [37] T. Flissikowski, A. Hundt, M. Lowisch, M. Rabe, and F. Henneberger, “Photon beats from a
431 single semiconductor quantum dot,” *Phys. Rev. Lett.* **86**, 3172 (2001).
- 432 [38] Niels Gregersen, Torben R. Nielsen, Julien Claudon, Jean-Michel Gérard, and Jes-
433 per Mørk, “Controlling the emission profile of a nanowire with a conical taper,”
434 *Opt. Lett.* **33**, 1693 (2008).
- 435 [39] I. Friedler, P. Lalanne, J. P. Hugonin, J. Claudon, J. M. Gérard, A. Beveratos, and I. Robert-
436 Philip, “Efficient photonic mirrors for semiconductor nanowires,” *Opt. Lett.* **33**, 2635 (2008).